Available online at www.sciencedirect.com

jmr&t Journal of Materials Research and Technology

journal homepage: www.elsevier.com/locate/jmrt

Original Article

Photo/piezo-catalytic performance of $0.5Ba(Zr_{0.2}Ti_{0.8})O_3$-$0.5(Ba_{0.7}Sr_{0.3})TiO_3$ ceramic

Shivam Dubey [a,1], *Akshay Gaur* [a,1], *Awad A. Ibraheem* [b,c], *Rahul Vaish* [a], *Anuruddh Kumar* [d,*], *Hyeong Kwang Benno Park* [e], *Yun Hwan Joo* [e], *Tae Hyun Sung* [e]

[a] *School of Mechanical and Materials Engineering, Indian Institute of Technology Mandi, Mandi, Himachal Pradesh 175005, India*

[b] *Physics Department, King Khalid University, Abha, Saudi Arabia*

[c] *Physics Department, Al-Azhar University, Assiut Branch, Assiut 71524, Egypt*

[d] *Center for Creative Convergence Education, Hanyang University, Seoul 04763, South Korea*

[e] *Department of Electrical Engineering, Hanyang University, 222, Wangsimni-ro, Seongdong-gu, Seoul 04763, South Korea*

ARTICLE INFO

Article history:
Received 25 October 2022
Accepted 11 January 2023
Available online 18 January 2023

Keywords:
Ferroelectric material
Piezocatalysis
Photocatalysis
Solar light
Indoor photocatalysis

ABSTRACT

0.5Ba $(Zr_{0.2}Ti_{0.8})O_3$-$0.5(Ba_{0.7}Sr_{0.3})TiO_3$ (BST-BZT) ceramic composition is known for exihibiting electrical properties. The present study brings out the prospective approach of utilizing well known BST-BZT ceramic composition for water cleaning application via piezocatalysis, photocatalysis and piezo-photocatalysis process. For this, BST-BZT ceramic composition was synthesized through solid state route reaction method and was characterized by scanning electron microscopy (SEM), X-ray diffraction (XRD), Raman spectroscopy and X-ray photoelectron spectroscopy (XPS). Methylene Blue (MB) a cationic dye was used as a representative organic pollutant, where the maximum degradation was observed in piezo-photocatalysis process (~92%) followed by photocatalysis process (~82%) and piezocatalysis process (~65%) in 240 min. Furthermore, the degradation of MB dye was examined under solar light irradiation in order to assess the potential of the BST-BZT ceramic composition. A study on the BST-BZT ceramic composition's photocatalytic activity in an indoor setting was also conducted. Finally, the phytotoxicity level of "*Vigna radiata*" seeds was examined to determine the extent of MB dye breakdown and its subsequent usage.

* Corresponding author.
E-mail address: anuruddh07@hanyang.ac.kr (A. Kumar).

[1] Both authors have contributed equally.

https://doi.org/10.1016/j.jmrt.2023.01.073

1. Introduction

With an exponential increase in the human population, there is an urgent need of environmental sustainability due to which the current research is highly focused on reusability, recyclability and reducibility. Particularly, sticking to water resources, our intentional or unintentional dumping of pollutants into the water bodies have degraded its quality [1]. Textile industries in itself consume a large fraction of water for its working and the used water (contaminated) is directly dumped into the river bodies [2]. The polluted water is not only dangerous for human but also the marine life gets affected which is one of the major constituents of our ecosystem [3]. Thus, it become upmost important to reuse this contaminated water by removing the harmful pollutants from it. However, in this regard, various solutions such as ion floatation, sedimentation, filtration, coagulation, adsorption etc., are widely accepted for water treatment [4–7]. These methods have their own challenges as most of them are less efficient, operating cost is high or sometimes the process results in inclusion of secondary toxic pollutants [8]. Photocatalysis is one of the advanced oxidation processes for water cleaning applications which has gained much popularity. Titanium oxide (TiO_2) is one of the most studied photocatalyst having high stability and superior electrochemical properties [9,10]. However, TiO_2 as a photocatalyst is been cornered due to its less visible light absorption capacity. Besides this recombination of the electron–hole pair results in surface defect effecting the efficiency of the energy conversion [11–13]. Surface functionalization, forming heterojunctions and tuning defects are however some of the strategies which can be employed to enhance the overall efficiency of the photocatalysis process [14,15]. Synthesis route of material also effects the efficiency of the any process such as traditional materials like Bi_2MoO_6, Co_3O_4 obtained in nano-scale synthesized through hydrothermal process showed excellent photocatalytic activities [16,17].

In the recent times, ferroelectric materials, with inbuilt spontaneous polarization are proved to be an effective photocatalyst in electrochemical processes. Ferroelectric materials such as $SrTiO_3$, $PbTiO_3$, $BaTiO_3$, and $BiFeO_3$ falls into such category [18–21]. Mechanical energy can be utilized for degrading the organic pollutants present in the water through piezocatalysis process. In piezocatalysis process, polarization is induced due to the mechanical strain (energy) whereas in conventional electrocatalytic process the electric potential is used to drive the electron [22]. Piezocatalyst having ability of the charge separation onto the surface when mechanical stress in the form of vibrations are applied can be utilized in water splitting, organic dyes, organic compound synthesis applications [23–26]. Ferroelectric materials such as $BaTiO_3$, $BiFeO_3$, $Pb(Zr_{0.52}Ti_{0.48})O_3$ etc. having inbuilt spontaneous polarization, which are employed for water cleaning application through piezocatalysis process [27–29]. Nevertheless, most piezoelectric materials have restricted charge carrier (electron–hole pair) due to weak conduction of electricity. This can be improved by perceptive attention of using piezoelectric material in photocatalysis process to achieve efficient organic pollutant degradation. It can be anticipated that if the piezocatalytic and photocatalytic characteristics of the ferroelectric material are coupled into single physical-chemical process, then the efficiency of the photocatalytic process will be enhanced by the piezo-driven separation of photogenerated electron–hole pairs.

Being a perovskite structure, ferroelectric $BaTiO_3$ based ceramics are generally given more attention due to its versatile characteristics. Calcium (Ca), Zirconium (Zr) and Strontium (Sr) are some common elements which are generally doped in $BaTiO_3$, and as a result these $BaTiO_3$ based ceramics have shown excellent multicatalytic properties (photocatalysis, piezocatalysis, and piezo-photocatalysis) in environmental remedies [30–32]. Doping Sr in $BaTiO_3$, increases the dielectric constant of the synthesized ceramics whereas similar trend of enhanced dielectric constant is been observed when Zr is doped replacing Titanium (Ti) lattice in $BaTiO_3$ ceramic [33,34].

As there are promising results of doping Sr and Zr in $BaTiO_3$ solid solution, multicatalytic properties of $BaTiO_3$ ceramic can be improved by introducing Sr and Zr elements simultaneously. Interestingly, Sr and Zr in $BaTiO_3$ solid solutions are also reported for excellent electrical properties [35,36]. Thus the present study focuses on the photocatalytic, piezocatalytic, and piezo-photocatalysis performance of $BaTiO_3$ based composition i. e, $0.5Ba(Zr_{0.2}Ti_{0.8})O_3$-$0.5(Ba_{0.7}Sr_{0.3})TiO_3$(BST–BZT). Due to its potential piezoelectric and ferroelectric capabilities, BST-BZT can be potential candidate for a key lead-free non-toxic piezoelectric material. However, its Curie temperature is not so high, so it cannot be treated a promising material in higher temperature applications. To the best of our knowledge, BST-BZT has not been explored for piezo/photo/piezo-photo catalytic activities for water cleaning application. Further, the composition was explored for photocatalysis performance under solar light source. At last degree of MB dye degradation was quantified by growing *"Vigna radiata"* seeds using treated water obtained from the piezo-photocatalysis process.

2. Experimental

2.1. Synthesis of BST-BZT composition

The BST-BZT composition was synthesized through solid state reaction route. The precursors were $BaCO_3$, ZrO_2, $SrCO_3$ and TiO_2 which were of analytical reagent grade (purity~99%). The precursors were manually mixed according to their stoichiometric ratio in mortar pestle for 45 min where the acetone was used a mixing medium. The obtained mixture was calcined at 1350 °C for at 6 h in Nabertherm (Germany) electric furnace.

2.2. Characterization

The phase formation of the synthesized BST-BZT composition was revealed from the X-ray diffraction data obtained from the Smart Lab X-ray diffractometer (Rigaku Corporation). The XRD data was recorded between 20 and 75° at a rate of 2°/minute. Further, the phase formed in the BST-BZT composition and the vibrational modes present were identified through Raman spectroscopy. For this, laser beam having

532 nm wavelength with 25 wt power having acquisition time of 10 s was pointed on the surface. For analyzing the surface morphology of the BST-BZT composition, synthesized powder was observed under the field emission scanning electron microscope (FE-SEM) (FEI SEM NOVA Nanosem 450, Hillsboro, OR). Further, for confirming the elements present in the BST-BZT composition, X-ray photoelectron spectroscopy (XPS technique) was employed using X-ray photoelectron spectrophotometer (NEXSA). The energy band gap of the synthesized BST-BZT composition was calculated from Tauc's plot through diffuse reflectance spectrum (DRS) facilitated in UV–visible spectrophotometer (SHIMADZU-2600). The degradation of the dye was also measured through UV–visible spectrophotometer.

2.3. Photocatalysis, piezocatalysis and piezo-photocatalysis experiments

For photocatalysis, piezocatalysis and piezo-photocatalysis experiments, initially 100 mg of BST-BZT powder (sample) was immersed in 10 ml of ~5 mg/L concentrated MB dye. The sample was powered by magnetic stirrer at 300 rpm for 6 h while keeping the temperature at 15 °C in the dark environment. In photocatalysis experiments, visible light source was obtained from 2 LEDs bulbs (15 W each, Havells) while for piezocatalysis experiments, ultrasonicator (40 kHz, 150 W) was utilized for generating stress–strain in the sample. In piezo-photocatalysis experiments, the two system i. e, piezocatalysis and photocatalysis setups were combined for conducting the experiments.

2.4. Photocatalysis under solar light

100 mg of BST-BZT was immersed in 10 ml of ~5 mg/L concentrated MB dye overnight at 300 rpm powered by a magnetic stirrer for attaining adsorption–desorption equilibrium. For solar-driven photocatalysis process, the solution containing BST-BZT sample was exposed directly to the sun in south campus, Indian Institute of Technology (IIT) Mandi on 12th February, 2022 (Saturday). The campus is situated in Himachal Pradesh (a state in India) at a height of ~1044 m (3425 feet) from sea level (Latitude:31°7744′ N, Longitude:76°9849' E). The atmospheric conditions were recorded as: 20-23 °C, atmospheric pressure 1014 mbar, wind speed 5 km/h towards northwest direction having relative humidity of 61%. For repeatability test, centrifuge device was used where the sample (catalyst and the degraded dye) was transferred to centrifuge tubes where it is rotated at high rpm for a specific time. The degraded dye is separated out by using a pipette and measured new tested dye is transferred to the centrifuge tube where it is shaked such that we have another tested sample (catalyst and new dye). The tested sample is now transferred to a beaker for performing repeatability test.

2.5. Photocatalysis under indoor irradiations

100 mg powder sample of BST-BZT was taken in 10 ml of MB dye having concentration of ~5 mg/L. Initially, the solution was kept for adsorption–desorption equilibrium on magnetic stirrer for around 6 h at 300 rpm in dark condition. Then for investigating indoor photocatalytic activity, MB dye containing BST-BZT sample was directly kept in closed room (open atmosphere) having an area of 150 square feet equipped with 4 tube lights (20 Watts each, Havells). Experiments were performed at night in order to avoid any solar light disturbance.

2.6. Phytotoxicity test

Phytotoxicity test was conducted on "*Vigna radiata*" seeds using MB dye having concentration 100 mg/L, 5 mg/L, treated water (obtained through piezo-photocatalysis process) and running tap water titled as W1, W2, W3 and W4 respectively. "*V. radiata*" seeds were purchased from local shop and were washed rigorously with water in order to get rid off the dust particles. Four lots having 10"*V. radiata*" seeds were kept in 15 ml glass vial (Borosil). Moisture content in the glass vials was maintained by keeping cotton bud beneath the "*V. radiata*" seeds. The seeds were kept in the dark environment for 15 days (temperature 20-26 °C in day and 2-8 °C at night time), where after every two days 1 ml of the W1, W2, W3 and W4 were pipette into the vials.

3. Results and discussion

Fig. 1 shows the XRD pattern obtained in a range of 20–80°. The peaks obtained were well matched with JCPDs No 05–0626. No extra peaks were formed in the synthesized BST-BZT composition revealing the complete doping of Sr and Zr in $BaTiO_3$ ceramic. The Raman spectrum of the synthesized BST-BZT composition was analyzed to confirm the phase formation. Fig. 2 shows Raman spectrum between 150 and 1000 cm^{-1} obtained by using 532 nm wavelength laser revealing the phase transition and structural changes of the BZT-BST ceramic. Dominating peaks in spectrum of BST-BZT composition are at ~247, ~307, ~514 and ~716 cm^{-1} at room temperature. Also, at ~180 wavenumber (cm^{-1}) a dip has been observed which is due to the A1 (TO2) anti-symmetry mode. The peaks at ~247 cm^{-1} and ~514 cm^{-1} are basically due to the transverse optical modes of A1 symmetry [37]. Whereas the peak at around ~307 cm^{-1} is due to B1 mode and ~716 cm^{-1} is as consequence of A1 (LO3)E (LO) mode confirming the tetragonal phase formed in BST-BZT composition [37,38].

Fig. 3(a), (b) and (c) show the surface morphology of the synthesized BST-BZT composition at 10,3 and 1 μm scale obtained from scanning electron microscope. It can be clearly seen that the morphology of BST-BZT composition have clusters which are irregular in shape with smooth edges. It is noted that size and shape of a particle governs the catalytic performance of the material. Also, the performance of catalysis can be effectively enhanced by tuning the nano/microstructures. However, for the first time BST-BZT composition is studied for catalysis, so the effect of microstructure on catalysis is not considered.

Fig. 4(a) shows the XPS survey of the synthesized BST-BZT composition in the range of 0–900 eV. XPS technique was employed to detect the elements present on the surface of BST-BZT composition. From Fig. 4(a), it can be seen that Barium (Ba), Strontium (Sr), Titanium (Ti), and Zirconium (Zr)

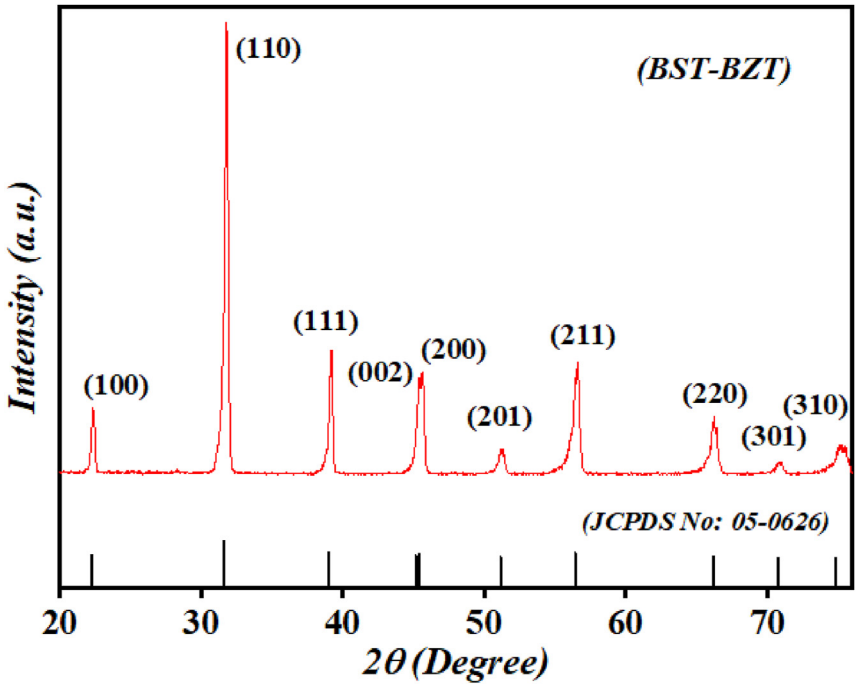

Fig. 1 – XRD pattern of BST-BZT powder.

were detected on the surface of BST-BZT composition. Further, in Fig. 4(b), the Ba spectrum was deconvoluted into 4 peaks where peaks at ~794.16 eV and ~778 eV are assigned due to the Ba atoms present in BST–BZT ceramics, and peaks at binding energy ~779.6 eV and ~795.18 eV can be attributed due to Ba atoms obtained during decomposition of carbonate layers of barium [39]. The Fig. 4(c) shows the Ti spectrum ~ 458 eV and ~463.6 eV which can be assigned to Ti2p3/2 and Ti2p1/2 orbitals showing Ti^{4+} cations [40]. Fig. 4(d) shows three peaks at ~528.97 eV, ~531.09 eV and ~532.83 eV which were obtained after deconvolution of O1s spectrum,

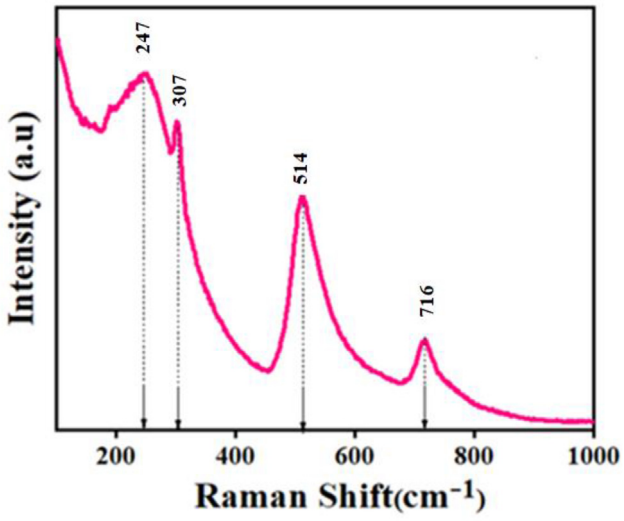

Fig. 2 – Raman spectrum of BST-BZT composition in range of 150–1000 cm^{-1}.

which can attributed to oxygen lattice, vacancy and absorbed oxygen respectively [41]. However, ~531.09 eV binding energy peak specifically does not resembles oxygen vacancy, but it can be also associated to absorbed O^-, O_2^-, and –OH groups [42,43]. Fig. 4(e) shows the orbitals peak of Zr at ~176.4 eV and ~178 eV representing 3d5/2 and 3d3/2 orbitals. The Sr spectrum can be deconvoluted into ~132.5 eV and ~134.32 eV binding energy as shown in Fig. 4(f). The absorbance spectrum of the synthesized sample in the range of 200–800 nm wavelength is shown in Fig. 5(a). The sample absorbs very less energy in the range of 550–800 nm wavelength, whereas there is gradually increment in the absorbance in range of 415–550 nm wavelength. After 415 nm wavelength there is a sudden rise in the absorption revealing the maximum absorption of the light in this particular range of wavelength. The energy band gap of the synthesized BST-BZT composition was calculated through Tauc's relation given by equation (1) [44,45].

$$\alpha(h\nu) = B(h\nu - Eg)\hat{}m \quad (1)$$

where, "B" is the energy independent coefficient, "α" is the coefficient of the absorption, "Eg" is the energy band gap of the synthesized sample, "h" is the plank's constant, "ν" is the frequency of the light and "m" represent the nature of the electronic transition responsible for optical absorption. For determining the direct and indirect energy band gap "m" is taken as 1/2 and 2 respectively. The energy band gap of the synthesized BST- BZT composition estimated by Tauc's plot is shown in Fig. 5(b). The value of the BST-BZT composition was found out to be ~3.19 eV. There is not much significant decrement in the band gap of the BST-BZT composition as the band gap of the tetragonal phase of the Barium titanate is ~3.2 eV [46]. The calculated energy band gap of the BST-BZT

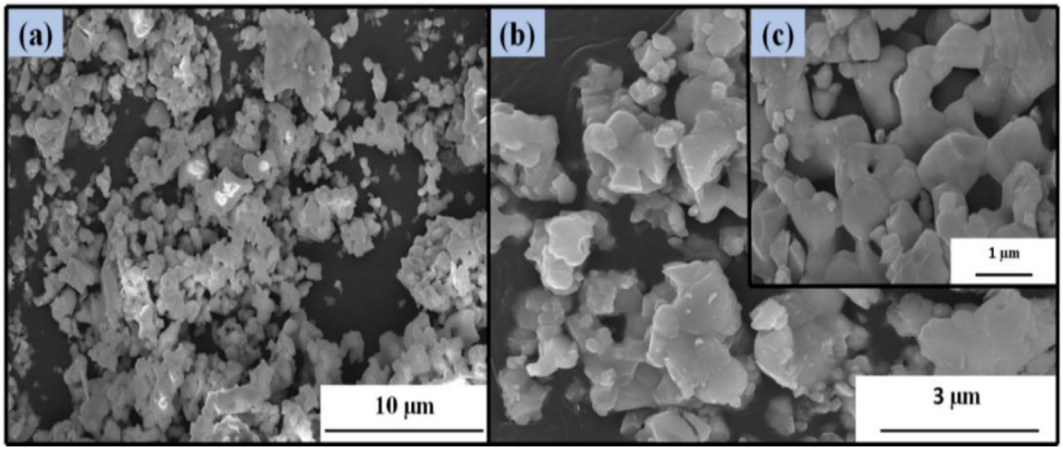

Fig. 3 – SEM images of BST-BZT powder.

composition i. e, 3.19 eV should only be limited to the ultraviolet region (100–400 nm wavelength) of the electromagnetic waves. However, when the BST-BZT composition was used as the photocatalyst for degradation of MB dye, a considerable amount of photoactivity under visible light source was observed. This can be due to gradual increment in absorption in the range of 415–550 nm wavelength as shown in Fig. 5(b).

Actually, for efficient photocatalysis process to occur numerous parameters such energy band gap, particle morphology and size, concentration of defects, crystallinity of synthesized materials, rate of recombination etc. plays an important role. However, in the present study, it is difficult to explain the full mechanism as well as the parameter responsible for showing the photocatalytic activity under visible light. Literature supports similar observations in few other materials. Cerium (Ce) doped Magnesium Oxide (MgO)is such an example having band gap higher than 3.0 eV showed excellent photoactivity, degrading phenol dye under visible light [47].

Fig. 6(a), (b) and (c) show the absorbance vs wavelength plots of photocatalysis, piezocatalysis and piezo-photocatalysis processes using 100 mg of BST-BZT composition for degrading 10 ml of ~5 mg/L concentrated MB dye. It can be clearly seen from the Fig. 6(a), (b) and (c) shows that the intensity of the absorption spectra is ~664 nm wavelength which decreased with time. Decrease in the intensity of the absorption spectra ~664 nm wavelength clearly indicates degradation of the MB dye. Fig. 6(d) shows the C/Co vs time plots depicting decrease in concentration of the MB dye under photocatalysis, piezocatalysis and piezo-photocatalysis processes. The degradation (D) (in %) of the MB dye is measured through using the following equation (2) [18].

$$D(in\ \%) = \left(\frac{Co - C}{Co}\right) * 100 \tag{2}$$

where, "Co" and "C" represent the initial concentration and concentration of MB dye at particular time.

Fig. 6(e) shows the kinetic performance of the MB dye using photocatalysis, piezocatalysis and piezo-photocatalysis processes. The kinetic study of MB dye degradation was analyzed through Langmuir–Hinshelwood model expressed in equation (3)-(4) [48].

$$Rate = -\left(\frac{dC}{dt}\right) = k\theta = \left(\frac{kKaC}{1}\right) + KaC \tag{3}$$

for very low concentration when $KaC << 1$

$$-\ln\left(\frac{C}{Co}\right) = Kt, \tag{4}$$

where, "k" and "Ka "represents the rate constant and adsorption coefficient of the reactant on the photocatalyst surface. Generally, the product of adsorption coefficient and concentration of dye is less than 1 i. e, $KaC << 1$ thus the kinetic rate (K in min^{-1}) becomes first ordered kinetic equation as shown in equation (4).

The values of kinetic rate constant (K) were found to be 0.0043 min^{-1}, 0.00647 min^{-1} and 0.00848 min^{-1} for peizocatalysis, photocatalysis and piezo-photocatalysis processes respectively for MB dye degradation using 100 mg of BST-BZT ceramic. It can be clearly observed from the spectra that maximum kinetic rate was found for piezo-photocatalysis process followed by photocatalysis and piezocatalysis processes. This implies more degradation extent compared to photocatalysis and piezocatalysis processes. The degradation of MB dye using 100 mg of BST-BZT ceramic was ~65, ~82 and ~92% through peizocatalysis, photocatalysis and piezo-photocatalysis processes in 240 min. The maximum degradation of MB dye obtained is basically due to the combined effect of both photocatalysis and piezocatalysis process.

A general photocatalysis, piezocatalysis and piezo-photocatalysis processes start with the adsorption of the dye onto the surface of the BST-BZT ceramic powder. Once the adsorption–desorption equilibrium is attained than the tested sample was exposed to visible light in photocatalysis process, mechanical vibrations were applied to the tested sample in dark environment whereas both mechanical vibrations and visible light source were subjected to piezo-photocatalysis process. In photocatalysis, when the light of the particular wavelength is subjected to photocatalyst the electron in the valence band gains enough energy that it leaves the valence

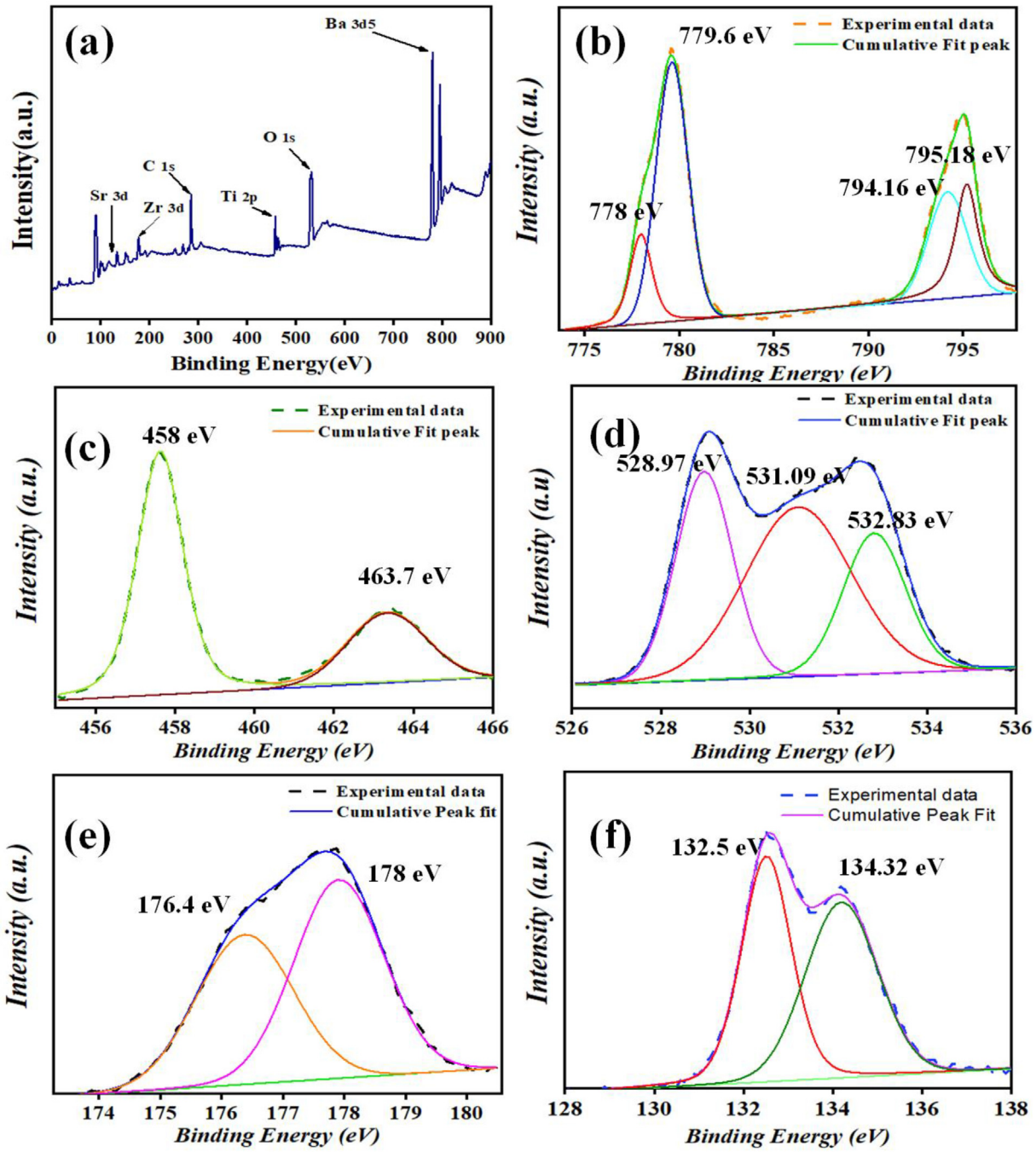

Fig. 4 – (a) XPS survey showing elemental composition in BST-BZT composition, (b) Ba3d spectrum, (c) Ti2p spectrum, (d) O1s spectrum, (e) Zr3d spectrum and (f) Sr3d spectrum.

band and enters the conduction band creating the equal number of holes in the valence band. This generated electron–hole pair reacts with water components present in the dye solution creating a reactive species which attacks the dye molecules. A schematic representation of photocatalysis under visible light is shown in Fig. 7(a), Also, a typical photocatalysis process is explained through following equations 5–10, [49].

Energy (visible source) → e^- (Conduction Band) / h^+ (Valance Band) (5)

$$H_2O + h^+ \rightarrow \bullet OH + H^+ \quad (6)$$

$$O_2\bullet^- + H^+ \rightarrow \bullet OOH \quad (7)$$

$$\bullet OOH + \bullet OOH \rightarrow H_2O_2 + O_2 \quad (8)$$

$$O_2\bullet^- + \text{pollutant} \rightarrow CO_2 + H_2O \quad (9)$$

$$\bullet OOH + \text{pollutant} \rightarrow CO_2 + H_2O \quad (10)$$

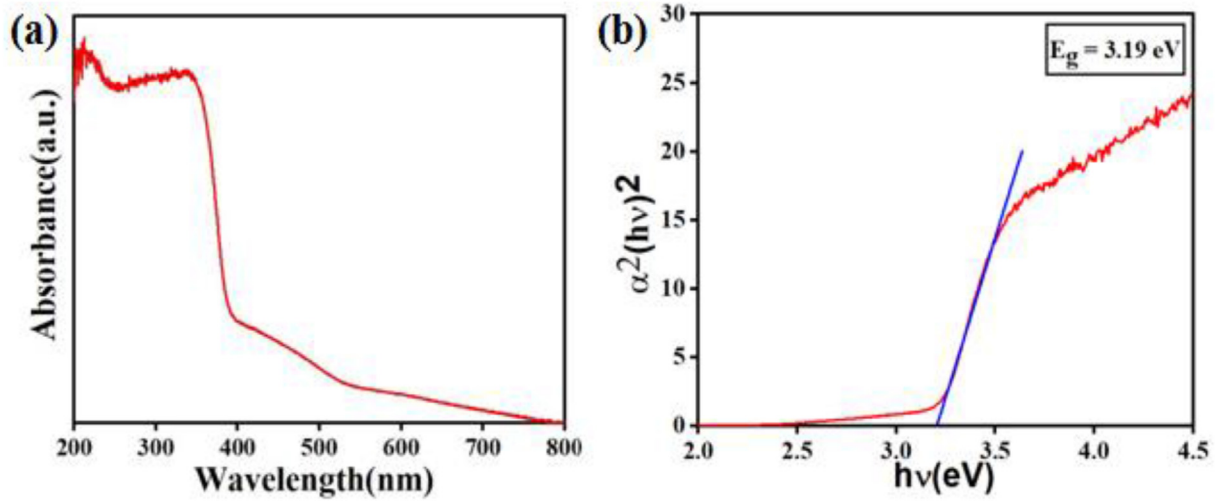

Fig. 5 – (a) Absorbance spectrum of BST-BZT composition in a range of 200–800 nm wavelength, (b) Tauc's plot showing energy band gap of BST-BZT composition.

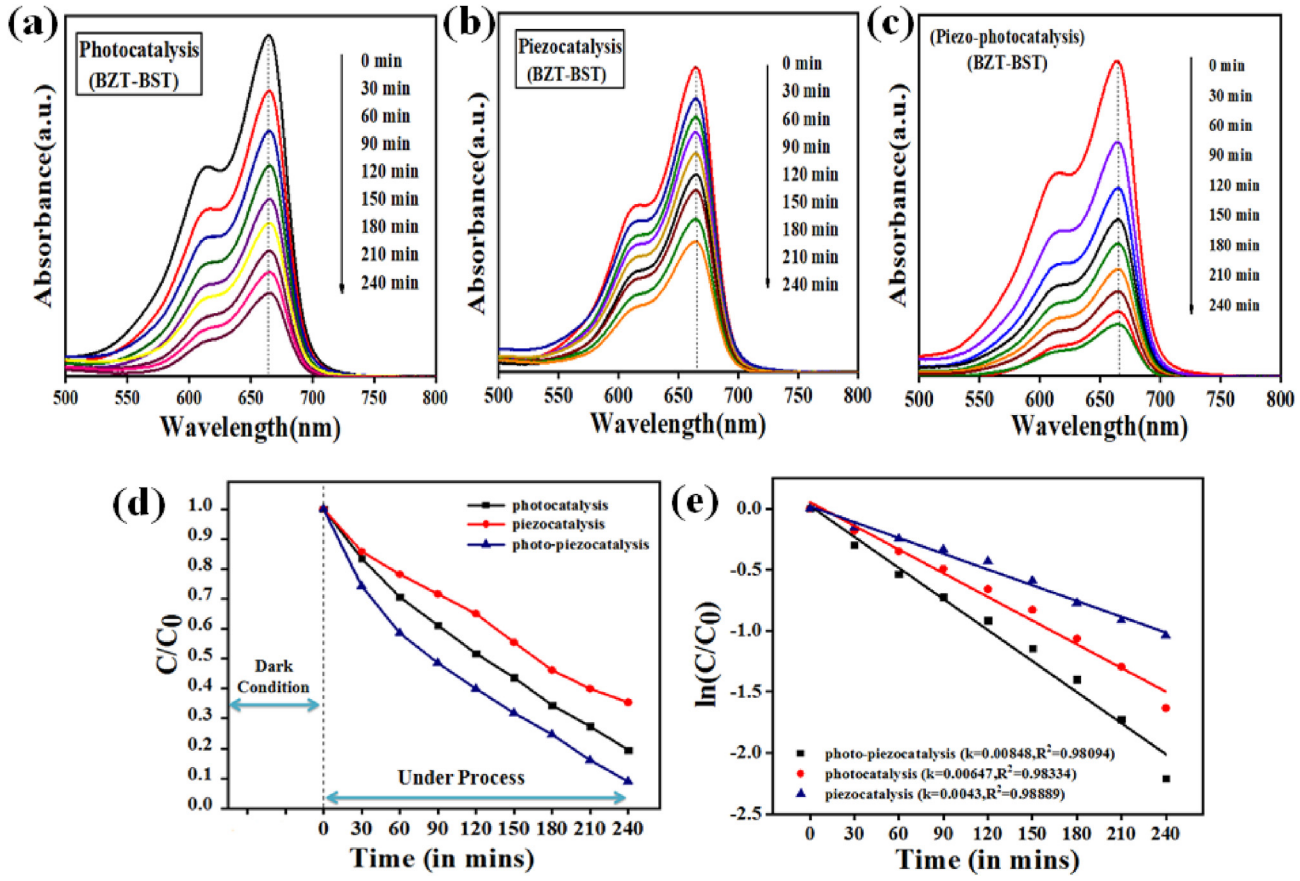

Fig. 6 – (a) Absorbance spectra of MB dye through photocatalysis process under visible light using 100 mg of BST-BZT composition, (b) Absorbance spectra of MB dye through piezocatalysis process using 100 mg of BST-BZT composition, (c) Absorbance spectrum of MB dye through combined effect of piezocatalysis and photocatalysis process i. e, piezo-photocatalysis process using 100 mg of BST-BZT composition, (d) C/Co vs time plot showing degradation of MB dye under photocatalysis, piezocatalysis and piezo-photocatalysis process, (e) Kinetic performance of MB dye under photocatalysis, piezocatalysis and piezo-photocatalysis process.

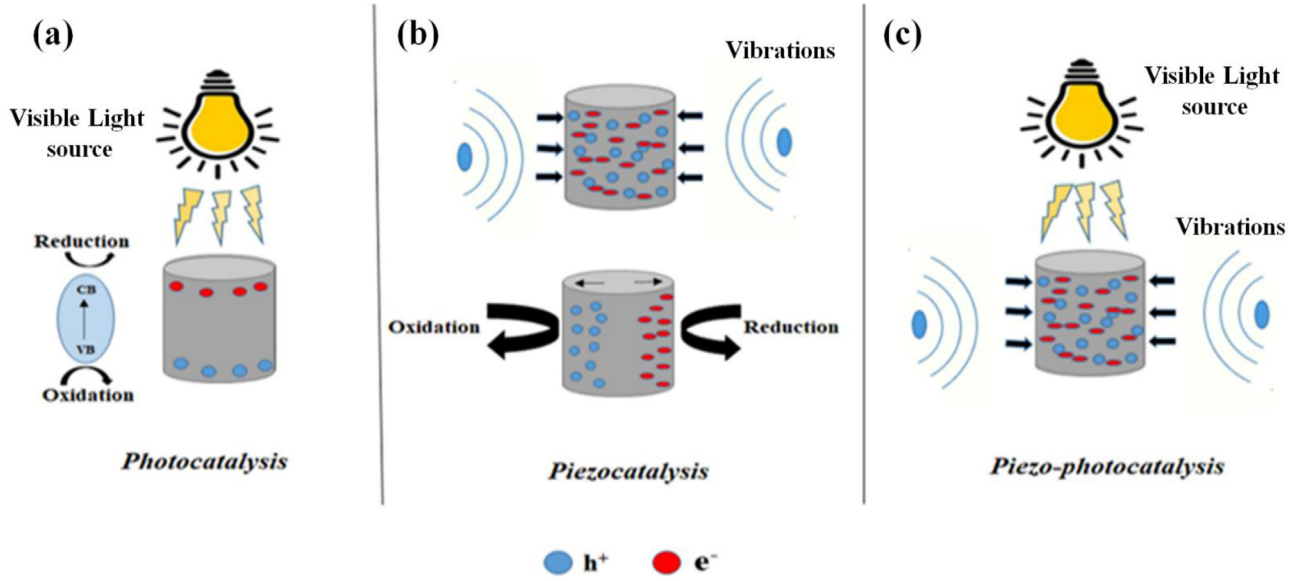

Fig. 7 – Schematic representation of processes (a) Photocatalysis, (b) Piezocatalysis and (c) Piezo-photocatalysis.

In piezocatalysis process, ultrasonicator produces the shock waves which exert pressure on the catalyst to produce direct piezoelectric effect in the synthesized samples contained within the dye. The positive charge (holes) and negative charge (free electron) generated due to direct piezoelectric effect results in the charge separation. These electron–hole pairs are the generated charge produced due to piezoelectric effect which takes part in redox reaction. It very interesting to know that during ultrasonication the cavities forms bubbles, which grows and ultimately bursts during ultrasonication. This formation/growth/collapse of the bubble leads to increase in localized temperature up to 4000–5000 K and generates shock wave up to ~10^8 Pa pressure [50]. Due to this discussed phenomenon called thermolysis (sonolysis) the degradation of the dyes may take place. However, in our present study when control reading without any synthesized sample was subjected to 4 h of ultrasonification a negligible amount of MB dye degradation was observed. Thus, degradation observed during ultrasonification was solely due to piezocatalysis process under vibrations. The end result of both photocatalysis and piezocatalysis process is same i. e, separation of charges, however the process of generation and separation of charges in both the charges are different. Also, the charge separated due to direct piezocatalysis process is not in free state unlike photocatalysis process. In piezocatalysis process, a continuous stress with varying amplitude must be applied as in the absence of the force else the recombination of charges will occur before performing oxidation and reduction process. A schematic representation of piezocatalysis process is shown in Fig. 7(b). A typical piezocatalysis process is been explained through following equations 11–16, [31].

$$\text{BST-BZT} + \text{vibrations} \rightarrow \text{BST-BZT}\ (h^+ + e^-) \quad (11)$$

$$e^- + O_2 \rightarrow O_2^{\cdot -} \quad (12)$$

$$h^+ + OH^- \rightarrow \cdot OH \quad (13)$$

$$2O_2^{\cdot -} + H^+ + H_2O \rightarrow H_2O_2 + O_2 + OH^- \quad (14)$$

$$H_2O_2 + O_2^{\cdot -} \rightarrow \cdot OH + OH^- + O_2 \quad (15)$$

$$\cdot OH\ (O_2^{\cdot -}) + \text{Dye molecule} \rightarrow \text{Decomposition} \quad (16)$$

Fig. 8 shows that even after the piezo-photocatalysis experiments there was no structure change in the synthesized BST-BZT ceramic powder which implies that BST-BZT can be used for repeatability test. In Fig. 9(a), it can be clearly seen that maximum degradation percentage of MB dye was found in piezo-photocatalysis process and followed by photocatalysis and piezocatalysis process. Actually, in the process like photocatalysis, piezocatalysis and piezo-photocatalysis, attacking species like holes (h^+), hydroxyl radicals ($\cdot OH$), electrons (e^-), and superoxide radicals ($\cdot O_2$) is been generated which is responsible for the degradation of the MB dye.

However, only one of the attacking species have dominating characteristics which is responsible for the degradation of dye. Particular scavenger traps specific attacking species, which means if that specific attacking species is been trapped than the dye degradation will not happen to that extent which was to be without that particular scavenger. The scavenger test was performed in order to identify the reactive species responsible for the degradation of MB dye. In the present study, scavenger test was performed in piezo-photocatalysis process by adding 1000 μL of Ethylene diaminetetra acetic acid (EDTA), Isopropanol (IPA) and Benzoquinone (BQ) scavengers to 10 ml of ~5 mg/L concentrated MB dye. Fig. 9 (b) shows ~32, ~26 and ~42% degradation of MB dye using scavenger EDTA, IPA and BQ respectively. Scavenger EDTA, IPA and BQ traps reactive species like. OH, h^+ and $\cdot O_2$ respectively [30]. From Fig. 9(b) it can be observed that among

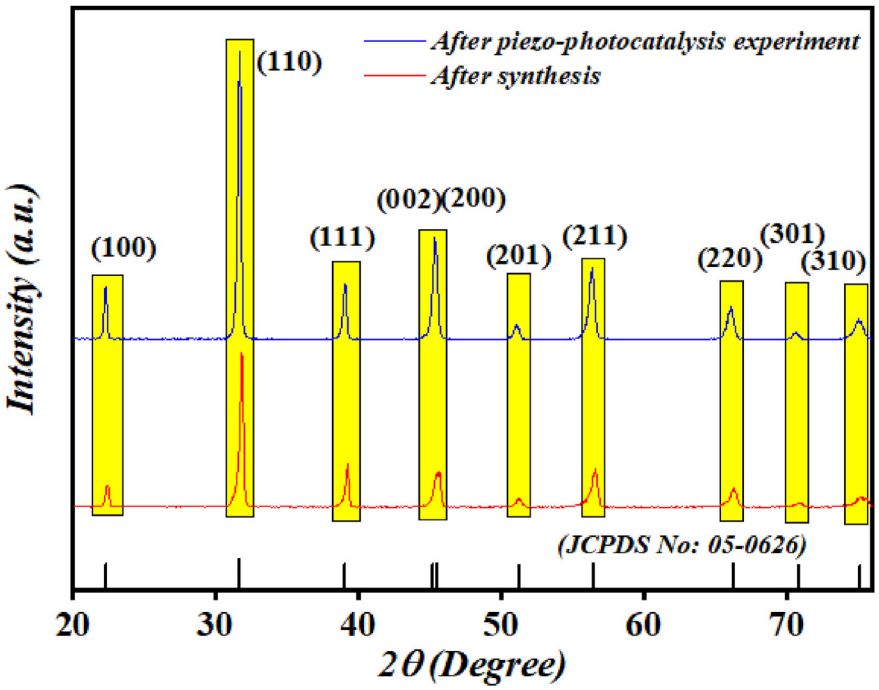

Fig. 8 – XRD patterns of BST-BZT composition before and after piezo-photocatalysis process.

all the scavengers, MB dye containing IPA have shown the minimum degradation indicating the minimum participation of. OH radical. This clearly indicates scavenger IPA trapped. OH radical which was the main responsible attacking species in piezo-photocatalysis process.

Further, to explore the catalytic properties of the synthesized BST-BZT composition, degradation of 10 ml–5 mg/L concentrated MB dye was attained in 120 min through photocatalysis process under sun light. Actually, the energy band gap of BST-BZT composition was ~3.19 eV which will correspond to UV range of light spectrum. Thus, it becomes essential to check the photocatalytic activity of the BST-BZT composition under real time solar light. A schematic representation of the photocatalysis process under the solar light is shown in the Fig. 10. Basically, sun light is an electromagnetic radiation comprising of majorly three types of bands i. e, infrared (700–1000 nm), visible (400–700 nm) and ultraviolet light (100–400 nm). When this sun light having such a wide range of wavelength falls onto the surface of the photocatalyst, the electron in the valance band corresponds to the energy of the falling photons. By this an equal number of holes is created in the valance band as a result of excitation of electron to the conduction band. This electron–hole pair participate in the redox reaction and as a result, degradation of MB dye starts. Fig. 11(a) shows the absorbance spectra of MB dye under solar light obtained in 120 min.

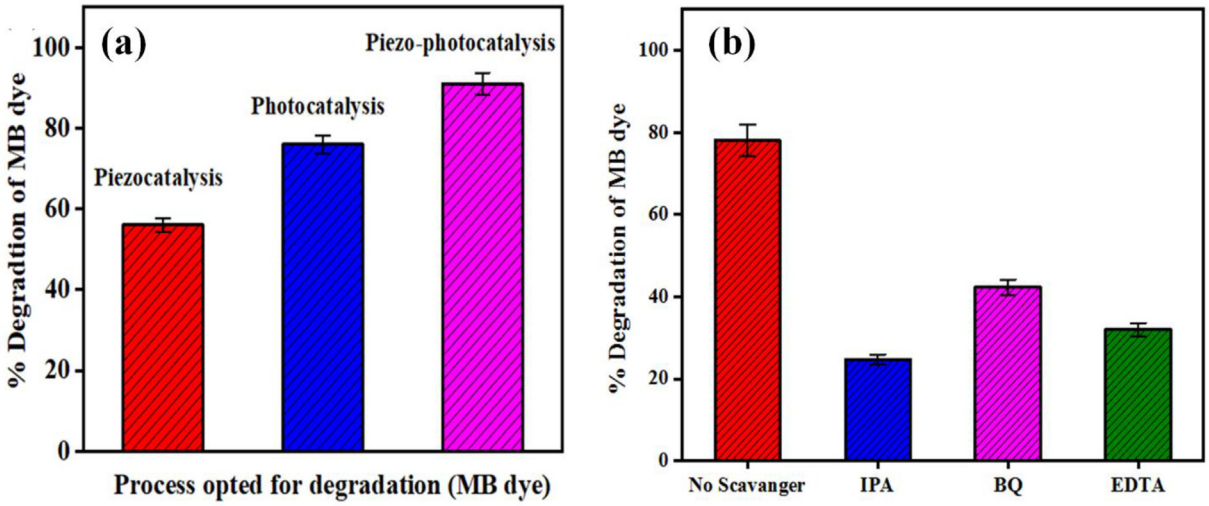

Fig. 9 – (a) Percentage degradation of MB dye using piezocatalysis, photocatalysis and piezo-photocatalysis process, (b) Scavenger test showing percentage degradation of MB dye through piezo-photocatalysis process.

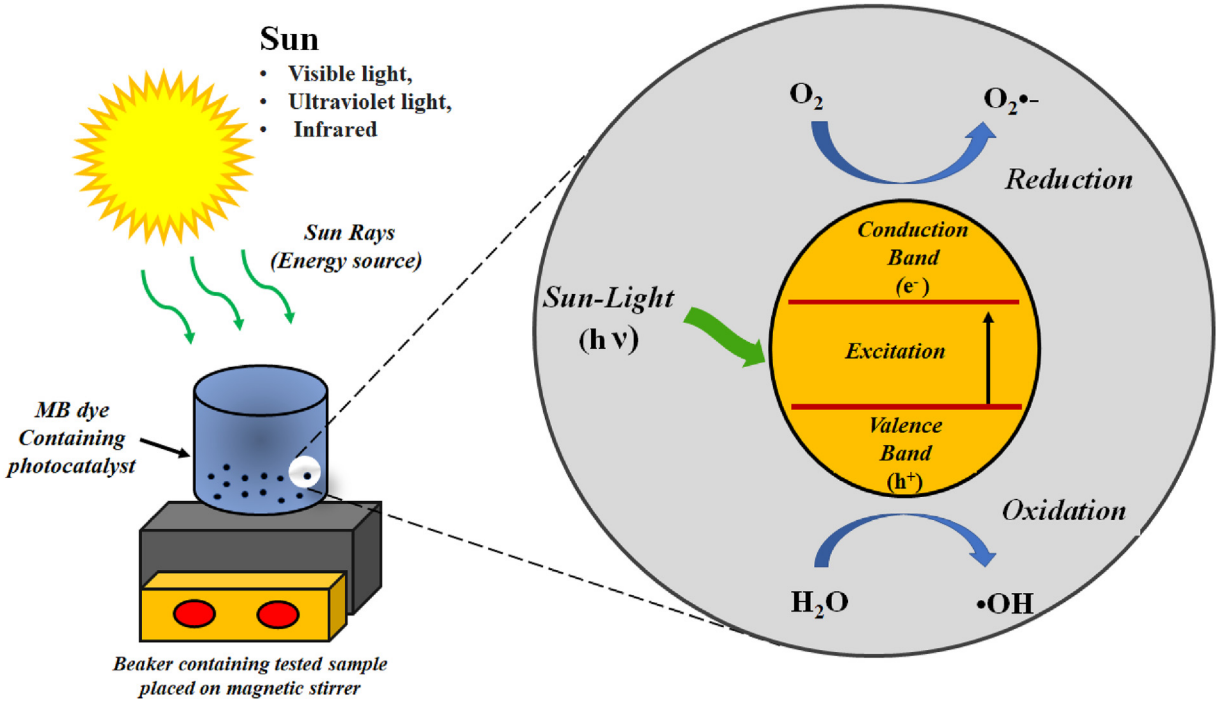

Fig. 10 – Schematic representation of photocatalysis process under real time solar conditions.

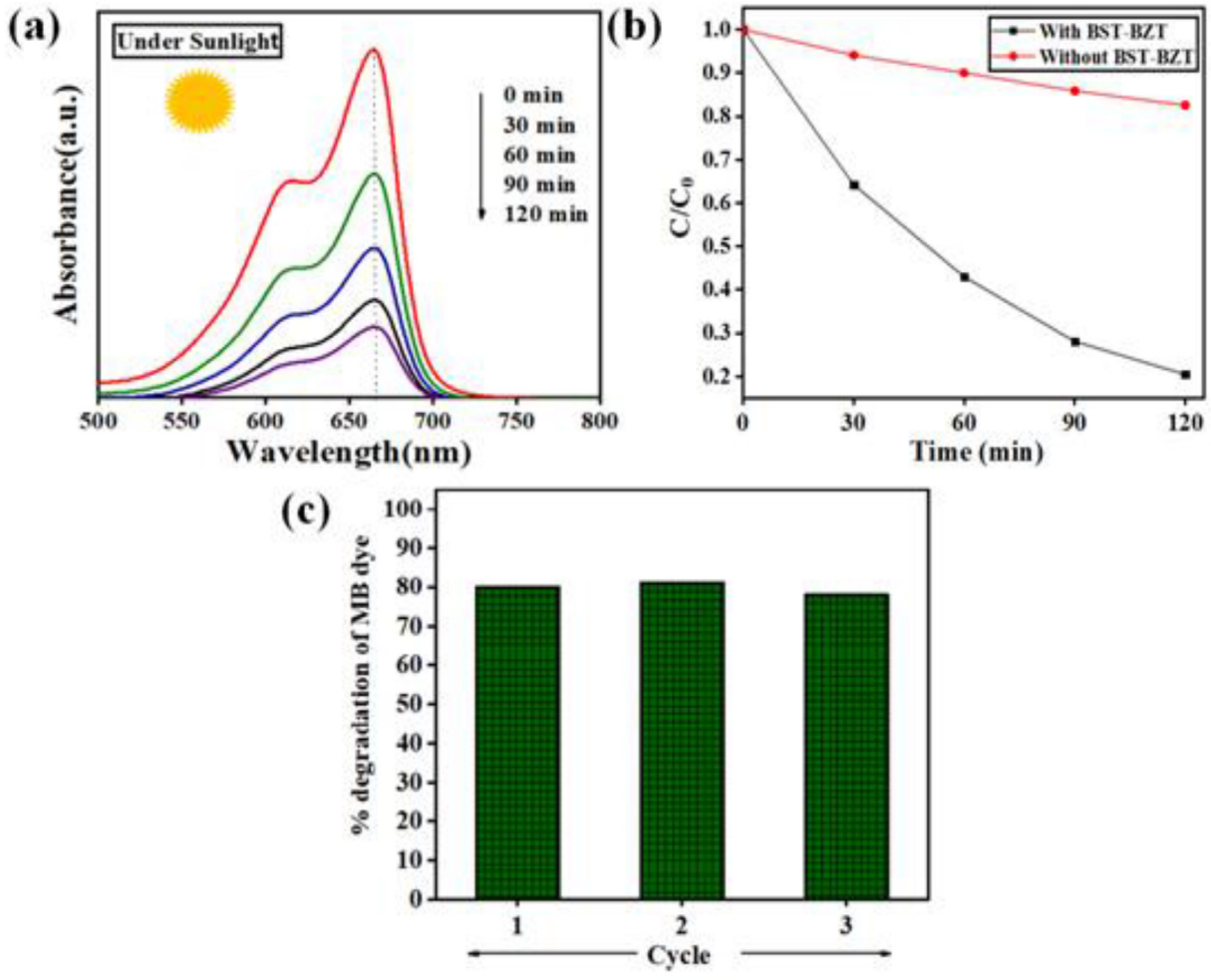

Fig. 11 – (a) Absorbance spectra of MB using BST-BZT under solar light, (b) C/Co vs time plot showing degradation MB dye, (c) Repeatability test.

Table 1 – Performance of ferroelectric photocatalyst under solar light.

S.No	Material	Pollutant	% Degradation
1.	$BiVO_4/SrTiO_3$ composite [51].	Sulfamethoxazole (10 mg/L)	~91%/60 min
2.	Ag–$BaTiO_3$ (Cubic)	Rhodamine B (10 mg/L)	~53%/60 min
	Ag–$BaTiO_3$ (Tetragonal) [52].		~100%/60 min
3.	$MnTiO_3$ nanoparticles [53].	Methylene Blue (10 mg/L)	~70%/240 min.
4.	$BaTiO_3/TiO_2$ composite [54].	Acetaminophen (5 mg/L)	~95%/240 min.
5.	$Na_{0.5}Bi_{2.5}Nb_2O_9$ nanosheets [55].	Rhodamine B, Methyl orange (20 mg/L)	~98, ~38%/120 min.
6.	$BaTiO_3$@g-C3N4 composites [56].	Methyl Orange (5 mg/L)	~76%/360 min.
7.	BST-BZT particles. [present study]	Methylene Blue (5 mg/L)	~80%/120 min

Further, Fig. 11(b) displays the C/C_0 vs time plot for showing the degradation achieved at particular time. For any ideal catalytic material, it is necessary that it should have a characteristic of repeatability and be used for several cycles without undergoing any change in its efficiency. Fig. 11(c) shows the repeatability performance of the synthesized BST-BZT under real time conditions where no significant change was observed in photocatalysis experiment in a span of 120 min for three cycles. So, it is very clear that BST-BZT composition can be used multiple times without any noticeable drop in performances. Some of the ferroelectric photocatalyst and their performance under solar light are listed in Table 1. Thus, synthesized BST-BZT provides cost effective ferroelectric ceramic obtained via solid state reaction method in micro-scale capable of performing multicatalytic properties.

Apart from the outdoor study (sunlight exposure) to our sample, the catalytic activity was observed under indoor light irradiation. Fig. 12(a) shows the absorbance spectra of MB dye degradation under indoor light in 6 h. Fig. 12(b) shows the C/C_0 vs time plots of MB dye degradation in indoor condition with and without BST-BZT. Interestingly, dye degradation was observed in real time indoor condition. As compared to reported data, BST-BZT has shown comparable performance. Some materials performing photocatalysis in indoor conditions are presented in Table 2.

The treated water obtained after degradation of MB dye through piezo-photocatalysis process was preserved in order to quantify the degree of organic pollutant removed. For this, seed germination test was conducted on "*V. radiata*" seeds where it was nourished with W1, W2, W3 and W4. Fig. 13 (a) shows 4 vials having germinated "*V. radiata*" seeds. The

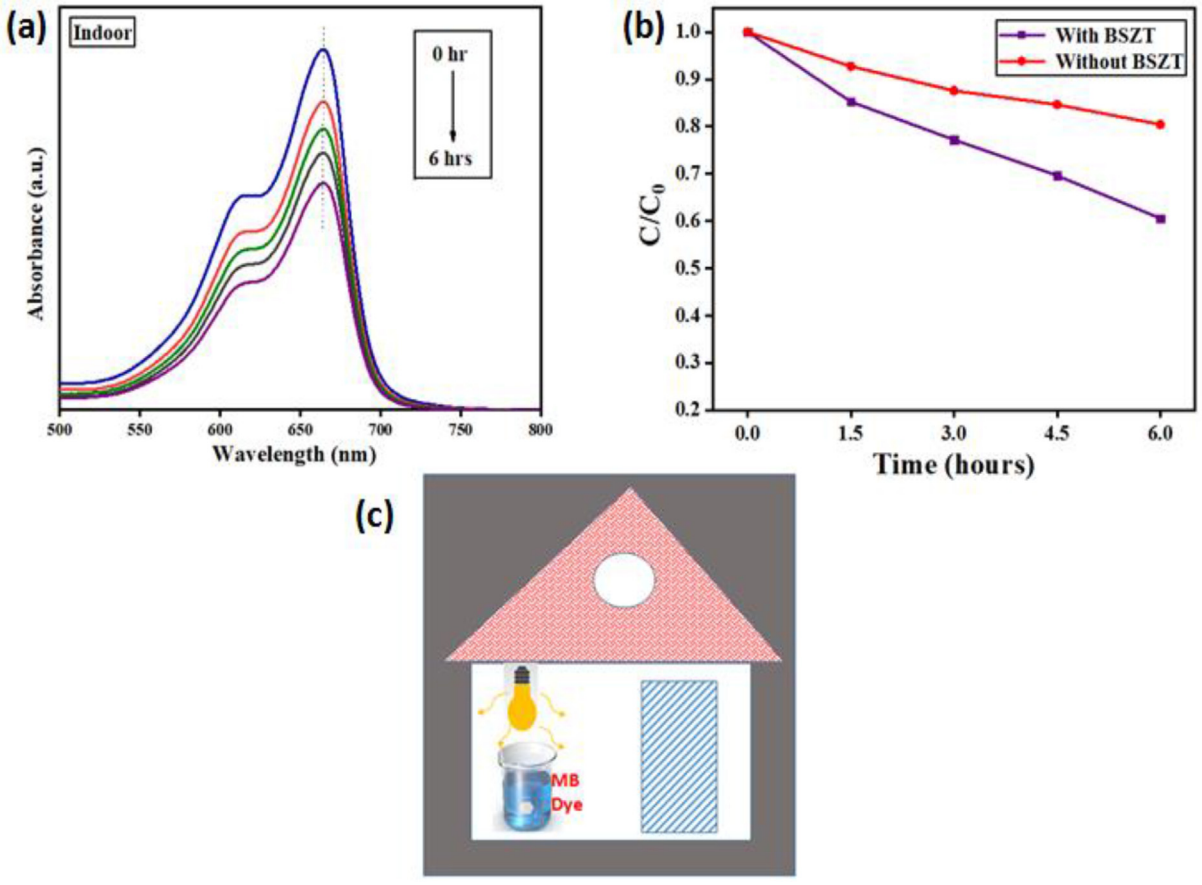

Fig. 12 – (a) Absorbance spectra of MB dye using BST-BZT under indoor condition, (b) C/Co vs time plots showing degradation MB dye, (c) Pictorial representation of MB dye been degraded in indoor conditions.

Table 2 – Indoor performance of various reported catalysis.

S. No.	Material	Pollutants	% Degradation/time
1.	Pure Ag_3PO_4 [57]	Rhodamine B	100%/36 h
2.	N-doped TiO_2 [57]	Rhodamine B	18%/120 h
3.	Pure Bi_2WO_6 [58]	Rhodamine B	30%/150min
4.	Zr–Er–Bi_2WO_6 [58]	Rhodamine B	100%/150 min
5	BST-BZT (present study)	Methylene Blue	42%/6 h

number of germinated "*V. radiata*" seeds and their respective length (in cm) were measured for estimating the germination index (GI) according to the equation [59]. The germination index obtained after using W1, W2 and W4 were used to compare phytotoxicity levels.

$$GI = \left(\frac{\text{Seed germination (\%)} \times \text{root treatments}}{\text{Seed germination (\%)} \times \text{root length of the control}}\right) \times 100 \quad (17)$$

The average length of germinated "*V. radiata*" seeds were ~1.8, ~2.3, ~4.5 and ~5.8 cm by using W1, W2, W3 and W4 respectively. High degree of toxicity will result in reduced length of germinated "*V. radiata*" seeds and its growth through treated water will account for the non-toxicity approach [60]. Fig. 13 (b) shows the germination index (GI) % of "*V. radiata*" seeds calculated after using W1, W2, W3 and W4. The values of the GI for "*V. radiata*" seeds using W1, W2, W3 and W4 were found out to be ~6.2, ~16.14, ~54.31 and ~90% respectively. The GI values can estimate phytotoxicity into three major levels, (i) high phytotoxicity (GI < 50%), (ii) moderate phytotoxicity 50% < *GI* < 80%, (iii) absence of phytotoxicity (GI > 80%) [61,62]. Clearly 100 mg/L and 5 mg/L concentrated MB dye fall under high toxicity whereas ~54% value of GI for "*V. radiata*" seeds using treated water i. e W3 showed moderate phytotoxicity.

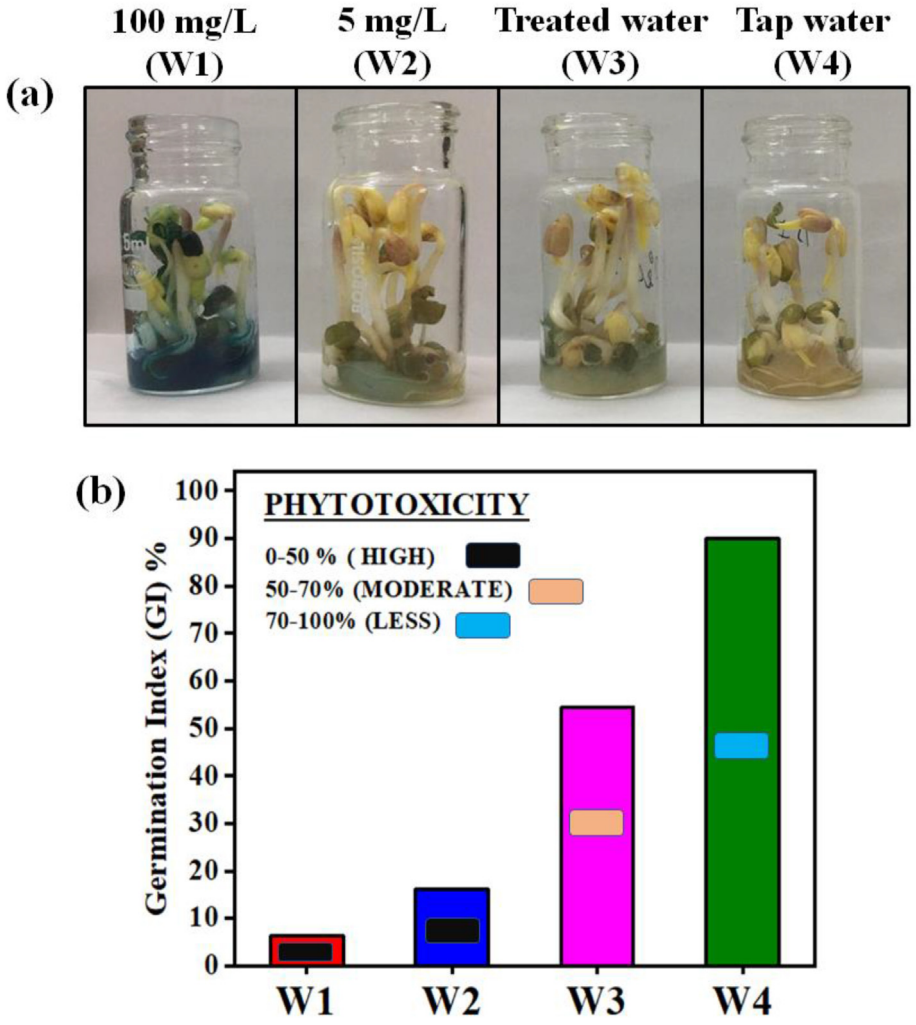

Fig. 13 – (a) 4 *Vials containing 10 green gram dal nourished by W1, W2, W3 and W4*, (b) *Germination Index (GI) showing the level of phytotoxicity*.

4. Conclusions

Ferroelectric ceramic composition $0.5Ba(Zr_{0.2}Ti_{0.8})O_3$-$0.5(Ba_{0.7}Sr_{0.3})TiO_3$(BST-BZT) was synthesized through solid state reaction route. The elements Sr and Zr were completely doped while maintaining the integrity of tetragonal $BaTiO_3$ ceramic. The composition was studied for multicatalytic performance i. e, piezocatalysis, photocatalysis and piezo-photocatalysis processes for degrading 10 ml of ~5 mg/L concentrated MB dye in 240 min. There was a remarkable ~92% degradation of the MB dye achieved through piezo-photocatalysis process due to combined effect of piezocatalysis and photocatalysis processes. The photocatalytic behavior of the BST-BZT ceramic was also analyzed under real time solar conditions where the degradation was found out to be ~80% in 120 min. In the same manner BST-BZT sample is also analyzed as a indoor catalyst for the degradation of MB dye in presence of only room light irradiations and it was found that around 42% degradation in 6 h. There was no significant change in the degradation of MB dye in three cycles while performing the photocatalysis process which revealed the repeatable characteristics of BST-BZT ceramic. Thus, from the present study it can be concluded that BST-BZT ceramic has multicatalytic ability in water cleaning application. Later, the Germination Index (GI) was calculated on "*V. radiata*" seeds using W3 which was found in the moderate phytotoxicity level.

Declaration of Competing Interest

The authors declare that they have no known competing financial interests or personal relationships that could have appeared to influence the work reported in this paper.

Acknowledgments

The authors extend their appreciation to the Deanship of Scientific Research at King Khalid University for funding this work through research groups program under grant number R.G.P.2/102/43. This work was supported by the Korea Institute of Energy Technology Evaluation and Planning (KETEP) and the Ministry of Trade, Industry & Energy (MOTIE) of the Republic of Korea (No. 20192010106790 and No. 20204010600090).

REFERENCES

[1] Boretti A, Rosa L. Reassessing the projections of the world water development report. NPJ Clean Water 2019;2(1):1–6.
[2] Chen L, Wang L, Wu X, Ding X. A process-level water conservation and pollution control performance evaluation tool of cleaner production technology in textile industry. J Clean Prod 2017;143:1137–43.
[3] Sall ML, Diaw AKD, Gningue-Sall D, Efremova Aaron S, Aaron J-J. Toxic heavy metals: impact on the environment and human health, and treatment with conducting organic polymers, a review. Environ Sci Pollut Res 2020;27(24):29927–42.
[4] Rauf MA, Qadri SM, Ashraf S, Al-Mansoori KM. Adsorption studies of Toluidine Blue from aqueous solutions onto gypsum. Chem Eng J 2009;150(1):90–5.
[5] Chong MN, Jin B, Chow CWK, Saint C. Recent developments in photocatalytic water treatment technology: a review. Water Res 2010;44(10):2997–3027.
[6] Colmenares JC, Luque R. Heterogeneous photocatalytic nanomaterials: prospects and challenges in selective transformations of biomass-derived compounds. Chem Soc Rev 2014;43(3):765–78.
[7] Madhavan J, Maruthamuthu P, Murugesan S, Anandan S. Kinetic studies on visible light-assisted degradation of acid red 88 in presence of metal-ion coupled oxone reagent. Appl Catal B Environ 2008;83(1–2):8–14.
[8] Gaya UI, Abdullah AH. Heterogeneous photocatalytic degradation of organic contaminants over titanium dioxide: a review of fundamentals, progress and problems. J Photochem Photobiol C Photochem Rev 2008;9(1):1–12.
[9] Ni M, Leung MKH, Leung DYC, Sumathy K. A review and recent developments in photocatalytic water-splitting using TiO2 for hydrogen production. Renew Sustain Energy Rev 2007;11(3):401–25.
[10] Xu H, Ouyang S, Liu L, Reunchan P, Umezawa N, Ye J. Recent advances in TiO 2-based photocatalysis. J Mater Chem 2014;2(32):12642–61.
[11] Qureshy AMMI, Ahmed M, Dincer I. Performance assessment study of photo-electro-chemical water-splitting reactor designs for hydrogen production. Int J Hydrogen Energy 2019;44(18):9237–47.
[12] Licht S, Wang B, Mukerji S, Soga T, Umeno M, Tributsch H. Efficient solar water splitting, exemplified by RuO2-catalyzed AlGaAs/Si photoelectrolysis. J Phys Chem B 2000;104(38):8920–4.
[13] Khan SUM, Al-Shahry M, Ingler Jr WB. Efficient photochemical water splitting by a chemically modified n-TiO2. 80- Science 2002;297(5590):2243–5.
[14] Yu Y, Zhang Z, Yin X, Kvit A, Liao Q, Kang Z, et al. Enhanced photoelectrochemical efficiency and stability using a conformal TiO2 film on a black silicon photoanode. Nat Energy 2017;2(6):1–7.
[15] Wang X, Li Z, Shi J, Yu Y. One-dimensional titanium dioxide nanomaterials: nanowires, nanorods, and nanobelts. Chem Rev 2014;114(19):9346–84.
[16] Dou R, Cheng H, Ma J, Qin Y, Kong Y, Komarneni S. Degradation of methylene blue by Co3O4 with activation of bisulfite. Funct Mater Lett 2020;13(3):2050016.
[17] Zhu B, Cheng H, Ma J, Qin Y, Kong Y, Komarneni S. Bi2MoO6 microspheres for the degradation of orange II by heterogeneous activation of persulfate under visible light. Mater Lett 2020;261:127099.
[18] Sharma M, Chauhan A, Vaish R. Energy harvesting using piezoelectric cementitious composites for water cleaning applications. Mater Res Bull 2021;137:111205.
[19] Huang X, Lei R, Yuan J, Gao F, Jiang C, Feng W, et al. Insight into the piezo-photo coupling effect of PbTiO3/CdS composites for piezo-photocatalytic hydrogen production. Appl Catal B Environ 2021;282:119586.
[20] Konta R, Ishii T, Kato H, Kudo A. Photocatalytic activities of noble metal ion doped SrTiO3 under visible light irradiation. J Phys Chem B 2004;108(26):8992–5.
[21] Niu F, Chen D, Qin L, Gao T, Zhang N, Wang S, et al. Synthesis of Pt/BiFeO3 heterostructured photocatalysts for highly efficient visible-light photocatalytic performances. Sol Energy Mater Sol Cells 2015;143:386–96.
[22] Liang Z, Yan C-F, Rtimi S, Bandara J. Piezoelectric materials for catalytic/photocatalytic removal of pollutants: recent advances and outlook. Appl Catal B Environ 2019;241:256–69.
[23] Hong K-S, Xu H, Konishi H, Li X. Piezoelectrochemical effect: a new mechanism for azo dye decolorization in aqueous

solution through vibrating piezoelectric microfibers. J Phys Chem C 2012;116(24):13045–51.
[24] Starr MB, Shi J, Wang X. Piezopotential-driven redox reactions at the surface of piezoelectric materials. Angew Chem Int Ed 2012;51(24):5962–6.
[25] Hong K-S, Xu H, Konishi H, Li X. Direct water splitting through vibrating piezoelectric microfibers in water. J Phys Chem Lett 2010;1(6):997–1002.
[26] Feng Y, Ling L, Wang Y, Xu Z, Cao F, Li H, et al. Engineering spherical lead zirconate titanate to explore the essence of piezo-catalysis. Nano Energy 2017;40:481–6.
[27] Lv W, Kong L, Lan S, Feng J, Xiong Y, Tian S. Enhancement effect in the piezoelectric degradation of organic pollutants by piezo-Fenton process. J Chem Technol Biotechnol 2017;92(1):152–6.
[28] You H, Jia Y, Wu Z, Xu X, Qian W, Xia Y, et al. Strong piezo-electrochemical effect of multiferroic BiFeO3 square micro-sheets for mechanocatalysis. Electrochem Commun 2017;79:55–8.
[29] Lin H, Wu Z, Jia Y, Li W, Zheng R-K, Luo H. Piezoelectrically induced mechano-catalytic effect for degradation of dye wastewater through vibrating Pb (Zr0. 52Ti0. 48) O3 fibers. Appl Phys Lett 2014;104(16):162907.
[30] Sharma M, Singh G, Vaish R. Dye degradation and bacterial disinfection using multicatalytic BaZr0. 02Ti0. 98O3 ceramics. J Am Ceram Soc 2020;103(9):4774–84.
[31] Sharma M, Vaish R. Piezo/pyro/photo-catalysis activities in Ba0.85Ca0.15(Ti0.9Zr0.1)1-xFexO3 ceramics. J Am Ceram Soc 2021 Jan 1;104(1):45–56.
[32] Qifeng L, Jingjun M, Sharma M, Vaish R. Photocatalytic, piezocatalytic, and piezo-photocatalytic effects in ferroelectric (Ba0. 875Ca0. 125)(Ti0. 95Sn0. 05) O_3 ceramics. J Am Ceram Soc 2019;102(10):5807–17.
[33] Weber U, Greuel G, Boettger U, Weber S, Hennings D, Waser R. Dielectric properties of Ba (Zr, Ti) O3-based ferroelectrics for capacitor applications. J Am Ceram Soc 2001;84(4):759–66.
[34] Huang K, Wang JB, Zhong XL, Liu BL, Chen T, Zhou YC. Significant polarization variation near room temperature of Ba0. 65Sr0. 35TiO3 thin films for pyroelectric energy harvesting. Sensor Actuator B Chem 2012;169:208–12.
[35] Patel S, Srikanth KS, Steiner S, Vaish R, Froemling T. Pyroelectric and impedance studies of the 0.5 Ba (Zr0. 2Ti0. 8) O3-0.5 (Ba0. 7Sr0. 3) TiO3 ceramics. Ceram Int 2018;44(17):21976–81.
[36] Patel S, Yadav H. Electrical conduction properties of the BZT–BST ceramics. J Adv Dielectr 2020;10(6):2050026.
[37] Hayashi H, Nakamura T, Ebina T. In-situ Raman spectroscopy of BaTiO3 particles for tetragonal–cubic transformation. J Phys Chem Solid 2013;74(7):957–62.
[38] Mondal T, Majee BP, Das S, Sinha TP, Middya TR, Badapanda T, et al. A comparative study on electrical conduction properties of Sr-substituted Ba1− x Sr x Zr0. 1Ti0. 9O3 (x= 0.00–0.15) ceramics. Ionics 2017;23(9):2405–16.
[39] Craciun V, Singh RK. Characteristics of the surface layer of barium strontium titanate thin films deposited by laser ablation. Appl Phys Lett 2000;76(14):1932–4.
[40] Nasser SA. X-ray photoelectron spectroscopy study on the composition and structure of BaTiO3 thin films deposited on silicon. Appl Surf Sci 2000;157(1–2):14–22.
[41] Kushwaha A, Aslam M. Hydrogen-incorporated ZnO nanowire films: stable and high electrical conductivity. J Phys D Appl Phys 2013;46(48):485104.
[42] Tabata K, Hirano Y, Suzuki E. XPS studies on the oxygen species of LaMn1− xCuxO3+ λ. Appl Catal Gen 1998;170(2):245–54.
[43] Dupin J-C, Gonbeau D, Vinatier P, Levasseur A. Systematic XPS studies of metal oxides, hydroxides and peroxides. Phys Chem Chem Phys 2000;2(6):1319–24.
[44] Singh G, Sharma M, Vaish R. Influence of LiNbO3 crystallization on the optical, dielectric and nanoindentation properties of the 30SiO2–35Li2O–35Nb2O5 glass. J Appl Phys 2019;126(21):214101.
[45] George A, Solomon S, Thomas JK, John A. Characterizations and electrical properties of ZrTiO4 ceramic. Mater Res Bull 2012;47(11):3141–7.
[46] Gaur A, Sharma M, Chauhan VS, Vaish R. Solar/visible light photocatalytic dye degradation using BaTi1− xFexO3 ceramics. J Am Ceram Soc 2022;105(8):5140–50.
[47] Srisuvetha VT, Rayar SL, Shanthi G. Role of cerium (Ce) dopant on structural, optical and photocatalytic properties of MgO nanoparticles by wet chemical route. J Mater Sci Mater Electron 2020;31(4):2799–808.
[48] Seddigi ZS, Ahmed SA, Ansari SP, Danish E, Abu Alkibash A, Ahmed S. Kinetics and photodegradation study of aqueous methyl tert-butyl ether using zinc oxide: the effect of particle size. Int J Photoenergy 2013;2013.
[49] Nuño M, Ball RJ, Bowen CR. Chapter Photocatalytic Properties of Commercially Available TiO2 Powders for Pollution Control. 2016.
[50] Singh G, Sharma M, Vaish R. Transparent ferroelectric glass–ceramics for wastewater treatment by piezocatalysis. Commun Mater 2020;1(1):1–8.
[51] Li J, Wang F, Meng L, Han M, Guo Y, Sun C. Controlled synthesis of BiVO4/SrTiO3 composite with enhanced sunlight-driven photofunctions for sulfamethoxazole removal. J Colloid Interface Sci 2017;485:116–22.
[52] Cui Y, Briscoe J, Dunn S. Effect of Ferroelectricity on Solar-Light-Driven Photocatalytic Activity of BaTiO3 Influence on the Carrier Separation and Stern Layer Formation. Chem Mater 2013;25(21):4215–23.
[53] Alkaykh S, Mbarek A, Ali-Shattle EE. Photocatalytic degradation of methylene blue dye in aqueous solution by MnTiO3 nanoparticles under sunlight irradiation. Heliyon 2020;6(4):e03663.
[54] Kurniawan TA, Yanyan L, Ouyang T, Albadarin AB, Walker G. BaTiO3/TiO2 composite-assisted photocatalytic degradation for removal of acetaminophen from synthetic wastewater under UV–vis irradiation. Mater Sci Semicond Process 2018;73:42–50.
[55] Lu L, Liang N, Li X, Sun H, Zhang Q, Hao X. Highly efficient synergetic piezo/photocatalytic degradation in novel M0. 5Bi2. 5Nb2O9 (M= Li, Na, K) ferroelectric nanosheets. Ceram Int 2021;47(6):8573–83.
[56] Xian T, Yang H, Di LJ, Dai JF. Enhanced photocatalytic activity of BaTiO3@ g-C3N4 for the degradation of methyl orange under simulated sunlight irradiation. J Alloys Compd 2015;622:1098–104.
[57] Teng F, Liu Z, Zhang A, Li M. Photocatalytic performances of Ag3PO4 polypods for degradation of dye pollutant under natural indoor weak light irradiation. Environ Sci Technol 2015;49(16):9489–94.
[58] Zhang Y, Ma Y, Liu Q, Jiang H, Wang Q, Qu D, et al. Synthesis of Er3+/Zn2+ co-doped Bi2WO6 with highly efficient photocatalytic performance under natural indoor weak light illumination. Ceram Int 2017;43(2):2598–605.
[59] Zeghioud H, Khellaf N, Amrane A, Djelal H, Bouhelassa M, Assadi AA, et al. Combining photocatalytic process and biological treatment for Reactive Green 12 degradation: optimization, mineralization, and phytotoxicity with seed germination. Environ Sci Pollut Res 2021;28(10):12490–9.
[60] Priac A, Badot P-M, Crini G. Treated wastewater phytotoxicity assessment using Lactuca sativa: focus on germination and root elongation test parameters. C R Biol 2017;340(3):188–94.
[61] Emino ER, Warman PR. Biological assay for compost quality. Compost Sci Util 2004;12(4):342–8.
[62] Zucconi F, Monaco A, Forte M, Bertoldi M de. Phytotoxins during the stabilization of organic matter. Compost Agric other wastes 1985. JKR Gasser.